Ultrathin nanoporous metal–semiconductor heterojunction photoanodes for visible light hydrogen evolution

Weiqing Zhang[1,§], Yunfeng Zhao[1,§], Kai He[1], Jun Luo[1,2], Guoliang Li[1,2], Ruirui Liu[1,2], Siyu Liu[1], Zhen Cao[1], Pengtao Jing[3], and Yi Ding[1,2] (✉)

[1] *Tianjin Key Laboratory of Advanced Functional Porous Materials, Institute for New Energy Materials & Low-Carbon Technologies, School of Materials Science and Engineering, Tianjin University of Technology, Tianjin 300384, China*

[2] *Center for Electron Microscopy, Tianjin University of Technology, Tianjin 300384, China*

[3] *State Key Laboratory of Luminescence and Applications, Changchun Institute of Optics, Fine Mechanics and Physics, Chinese Academy of Sciences, Changchun 130033, China*

[§] *Weiqing Zhang and Yunfeng Zhao contributed equally to this work.*

ABSTRACT

Plasmonic metal–semiconductor nano-heterojunctions (NHJs), with their superior photocatalytic performance, provide opportunities for the efficient utilization of solar energy. However, scientific significance and technical challenges remain in the development of suitable metal–semiconductor NHJ photoelectrodes for new generation flexible optoelectronic devices, which often require complex processing. Herein, we report integrated three-dimensional (3D) NHJ photoelectrodes by conformally coating cadmium sulfide (CdS) nanolayers onto ultrathin nano-porous gold (NPG) films via a facile electrodeposition method. Localized surface plasmon resonance (LSPR) of NPG enhances the electron–hole pair generation and separation. Moreover, the direct contact interface and high conductive framework structure of the NHJs boosts the photogenerated carrier separation and transport. Hence, the NHJs exhibit evidently enhanced photocurrent density and hydrogen evolution rate relative to CdS deposited on either gold (Au) foil or fluorine-doped tin oxide (FTO) at 0 V vs. SCE (saturated calomel electrode) under visible-light irradiation. Moreover, they demonstrate a surprisingly stable photoelectrochemical hydrogen evolution (PEC-HE) activity over 104 s of continuous irradiation.

1 Introduction

Photoelectrochemical (PEC) water splitting, the conversion of solar energy into clean hydrogen fuel, is deemed as one of the most promising strategies for addressing the global energy and environmental crisis [1–3]. At present, the overall energy conversion efficiency of PEC technologies is far below what is

required for practical use. This shortcoming is primarily attributed to the low efficiency of the three fundamental steps of the PEC water splitting process: sunlight absorption, electron–hole pair separation and transport, and surface redox reactions. To address these issues, in addition to the early development of single-component semiconductor materials, significant efforts have been devoted to the development of semiconductor nano-heterojunctions (NHJs) due to their improved photocatalytic activities [4, 5]. Thus far, a variety of semiconductor-based heterojunctions have been explored, including semiconductor–semiconductor (S–S) [6–9], semiconductor-metal (S–M) [10–13], and semiconductor–carbon [14–16] heterojunctions. In particular, plasmonic S–M NHJs have emerged as promising photocatalysts because the photonic and plasmon–exciton coupling effects between a metal and a semiconductor give rise to many advantageous optical and electrical characteristics, such as: (1) enlarging the absorption cross sections [17]; (2) increasing the effective average optical path length [18, 19]; (3) producing an intense electromagnetic near-field (E-field) [20]; and (4) transferring the energy stored in the local plasmonic field from the metal nanostructures to the semiconductor nanomaterials [21, 22]. These virtues facilitate the generation, separation, and transport of electron–hole pairs, thus improving the photon-to-hydrogen conversion efficiency [17, 23–24]. As a paradigm in S–M NHJ systems, heterojunctions consisting of cadmium sulfide (CdS) with plasmonic metal nanoparticles have been demonstrated to be optimal candidates for visible-light-driven water splitting [25–27]. This is because CdS possesses a suitable band gap (~2.4 eV) and conduction band (CB) edge (−0.52 eV) [21, 28], which guarantee visible-light-driven PEC hydrogen evolution (PEC-HE). Upon further combination of CdS with plasmonic metals such as gold (Au), the produced light trapping and plasmon–exciton coupling effects can significantly improve the PEC-HE performance [17, 20, 29].

Recently, three-dimensional (3D) photoelectrodes, including 1D arrays and 3D interconnected porous nanostructures, have shown intriguing performance for PEC water splitting by promoting light absorption and charge-carrier transport [30–33]. Relative to 1D arrays, 3D interconnected porous structures exhibit a larger accessible surface area, which can greatly shorten the electron pathways and thus decrease the possibility of electron–hole recombination [34, 35]. While most reported 3D photoelectrodes are based on 1D arrays, 3D interconnected porous structures, especially with sub-micron thickness, have rarely been reported. Herein, we report an effective 3D interconnected NHJ photoelectrode with a CdS nanolayer (NL) conformally coated on a nanoporous gold (NPG) film (abbreviated as 3D NPG/CdS NHJ). By taking advantage of the properties of NPG and NPG/CdS NHJ (the localized surface plasmon resonance (LSPR) and highly conductive 3D framework of NPG, and the direct contact interface of NHJ), the charge-carrier formation, separation and transport behavior of these NPG/CdS NHJ photoelectrodes can be significantly improved. Specifically, the proposed NHJ photoelectrodes can achieve a photocurrent density of 1.04 mA·cm^{-2} and a hydrogen evolution rate of 406 mmol·h^{-1}·g^{-1} at 0 V vs. SCE (saturated calomel electrode) under visible-light irradiation at an overall electrode thickness of just ~100 nm; these values are 2- and 4-fold larger than those for the same amount of CdS deposited on gold foil (abbreviated as Au/CdS) and fluorine-doped tin oxide substrates (abbreviated as FTO/CdS), respectively. More importantly, the NPG/CdS NHJ photoanodes show surprising photostability compared with bare CdS, which is known to suffer tremendous photo-corrosion under illumination. Furthermore, the obtained photoelectrodes are flexible and can be easily mass produced, which make them favorable for practical PEC water splitting.

2   Experimental

2.1   Synthesis and fabrication of NPG/CdS, planar Au/CdS, and CdS photoanodes

NPG was prepared by dealloying 100 nm $Au_{50}Ag_{50}$ (at.%) alloy nanofilms in HNO_3 (67%) for 30 min at 30 °C. After dealloying, the NPG was washed 3–4 times with ultrapure water and carefully adhered to a clean polyethylene terephthalate (PET) film by the lift-coating method (as illustrated in Fig. S1 in the Electronic Supplementary Material (ESM)). Then, a thin Au foil was overlapped with one side of the NPG to serve as a conductor, and the electrodeposition

area of the NPG was restricted to 1 cm^2 with tape. For electrodeposition of CdS, 50 mM Cd(NO$_3$)$_2$·4H$_2$O and elemental S (64 mg) were dissolved in dimethyl sulfoxide (DMSO) at 50 °C, and a constant cathodic current of 0.5 mA·cm^{-2} was applied to the NPG electrode. High-purity N$_2$ was bubbled through the solution for at least 15 min before the experiment and was maintained throughout the procedure in order to create an N$_2$ atmosphere. For the electrodeposition of CdS onto planar Au or FTO, the procedure was identical to that described above, except that the NPG was replaced with Au foil or FTO.

2.2 PEC-HE performance measurements

PEC-HE activity measurements were performed in a homemade PEC cell (Fig. S2 in the ESM), a three-electrode system with a Pt plate as the counter electrode, an SCE with a double salt bridge as the reference electrode, and the as-prepared photoanode as the working electrode. An electrochemical analyzer (CHI760D) was used to measure the PEC-HE activities of the samples. In this study, the photocatalytic experiments were conducted under visible-light irradiation from a Xe lamp (420 nm < λ < 780 nm, 100 mW·cm^{-2}), and the potentials were recorded relative to the SCE. The hydrogen evolution process was monitored by a gas chromatograph with a thermal conductivity detector (GC-TCD). Once the sample and N$_2$-saturated 0.1 M Na$_2$S were loaded, the reaction cell was closed and connected to a 2 mL·min^{-1} nitrogen line and the GC-TCD. The purging process was applied to the cell for at least 15 min while the solution was stirred. Once illumination was begun, gas samples were automatically drawn for measurement every 10 min. A stable hydrogen peak was then integrated to calculate the evolution rate. The reaction temperature was maintained at room temperature using condensate water.

2.3 Characterization of photoelectrode materials

The morphologies of the NPG/CdS electrodes were investigated using a Verios 460L ultrahigh-resolution scanning electron microscopy (SEM) instrument. The composition of the NHJ was analyzed using an Oxford INCA X-Sight energy-dispersive X-ray spectroscopy (EDS) apparatus. The microstructures and compositions

of the samples were characterized using JEOL JEM-2100 and JEM-2100F transmission electron microscopy (TEM) systems operating at 200 kV, and an FEI Titan Themis 300 STEM system operating at 200 kV equipped with spherical aberration (Cs) correctors for both the probe- and image-forming objective lenses. The probe convergence angle was 21 mrad. The ultraviolet visible (UV-Vis) absorption spectra and diffuse reflectance spectra were obtained using Shimadzu UV-1700 and UV-2550 spectrophotometers, respectively. The chemical statuses and electronic states of the elements were investigated using an X-ray photoelectron spectroscopy (XPS) instrument (ESCALAB 250Xi, ThermoFisher). The electrodeposition procedure and PEC-HE activity were carried out on an electrochemical workstation (CHI760D). Electrochemical impedance spectroscopy (EIS) was performed on a Princeton electrochemical workstation operating in a frequency range of 5 kHz to 50 mHz. Incident photon-to-electron conversion efficiency (IPCE) measurements were conducted on a CIMPS-QE/IPCE system at a constant bias (0 V vs. SCE). Transient absorption spectroscopy measurements were obtained using a Ti:sapphire laser (Spectra-Physics, Spitfire ACE, 800 nm, 4.5 mJ/pulse, FWHM 35 fs, 1 kHz). Electron energy loss spectroscopy (EELS) experiments were carried out in an FEI Titan Themis G2 (S)TEM operated at 200 kV. The measured energy resolution (defined as the full width at half-maximum of the zero-loss peak) is better than 200 meV.

3 Results and discussion

Nanostructured Au/CdS NHJs are often prepared by depositing CdS onto the surfaces of Au nanostructures via a wet-chemical process using ligands and polymers as bridge molecules because of the strong lattice mismatch between Au and CdS [21, 36]. From the perspective of the photocatalysis process, however, the existence of bridge molecules may hinder the transport of charge carriers and aggravate thermodynamic and kinetic energy losses [37]. In the present work, CdS was directly electrodeposited onto the surface of NPG through interfacial electron transfer instead of using bridge molecules (see Fig. 1(a)), thereby promoting the charge-carrier transfer process. In the NHJs, NPG films are expected to play important roles
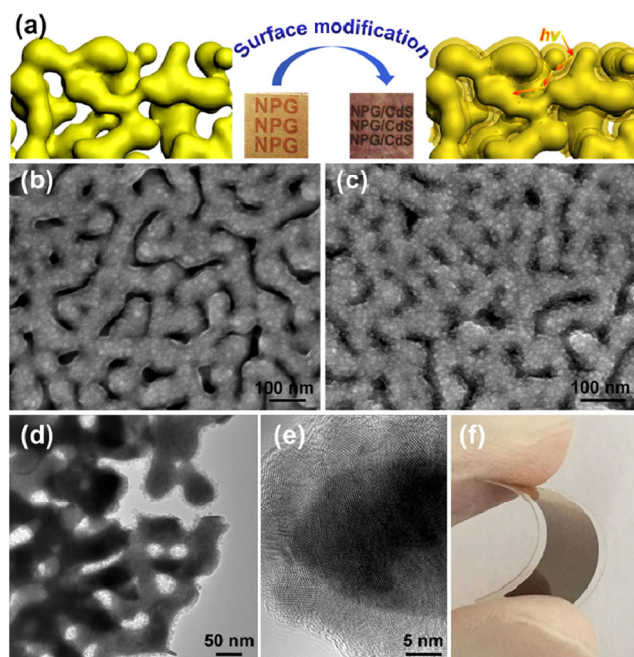
Figure 1 (a) Schematic illustration of NPG before and after electrodeposition of the CdS nanolayer. (b) and (c) FESEM images of NPG/CdS structures produced with an electrodeposition time of (b) 60 s and (c) 110 s. (d) and (e) TEM images of an NPG/CdS structure produced with an electrodeposition time of 60 s. (f) Digital photograph of an NPG/CdS photoelectrode under bending.

in photocatalysis because they are endowed with a significant LSPR phenomenon and 3D network nano-structure [38, 39]. It is well known that the LSPRs of plasmonic metals can improve the efficiency of solar light harvesting and generate an intense E-field at the surface of metals [22, 40]. The presence of many nanopores (also known as "hot-spot") in NPGs, further enhances the E-field around the surface of NPG via the electromagnetic coupling effect [41, 42]. Once CdS is combined with NPG, it would be subjected to strong interference from the LSPR of NPG [20, 43], and the resulting S–M NHJs could exhibit impressive photocatalytic performances.

SEM images (Figs. S3(a) and S3(b) in the ESM) show that NPG possesses a bi-continuous porous nanostructure with an average pore size of ~25 nm. ssConsidering that the NPG is as thin as ~100 nm, with a high porosity of over 60%, there are only 2–3 porous layers across its thickness [44, 45]. Therefore, the NPG film is translucent regardless of whether it is coated with CdS (see the insert of Fig. 1(a)). This feature is desirable for the potential application of

such films in photoelectric systems. After just 60 s of electrodeposition, SEM images (Fig. 1(b) and Fig. S3(c) in the ESM) show evidently coarsened ligaments compared with bare NPG, indicative of successful coating with a CdS NL. When the electrodeposition time is increased to 110 s, the roughness and thickness of the ligaments increase, but the nanoporous structure is still preserved (Fig. 1(c) and Fig. S3(d) in the ESM). The SEM images of these NPG/CdS NHJs at low magnification also do not reveal large CdS nano-particles on the surfaces (Figs. S3(c) and S3(d) in the ESM), which suggests that the CdS NL is evenly deposited on the surfaces of all the ligaments of the NPG. The structure of the NPG/CdS NHJs is further confirmed by TEM. As shown in Fig. 1(d), the interconnected NPG ligaments are uniformly covered by a CdS NL with a thickness of ~8 nm when the electrodeposition time is 60 s, consistent with the SEM observations. Corresponding high-resolution TEM (HRTEM) images from a random region of the NPG/CdS structure (Fig. 1(e)) show that the conformal coating exhibits good crystallinity and that the CdS nanoparticles are compactly assembled on the NPG surface in a highly uniform manner. By varying the electrodeposition time from 40 to 140 s, the thickness of the CdS NL on the NPG ligaments can be precisely tuned from ~5 to ~20 nm (Fig. S4 in the ESM). The corresponding EDS analysis shows that the molar ratio of Cd to S is approximately 1:1 in the NPG/CdS (Fig. S5(a) in the ESM). XPS reveals Cd MNN Auger peaks, which are exclusively assigned to CdS (Fig. S5(b) in the ESM). More interestingly, the NPG/CdS NHJs prepared on PET substrates in this study display both excellent flexibility and mechanical rigidity (Fig. 1(f)), which are beneficial for the maneuverability of the PEC cells.

The state of the NPG/CdS NHJ interface plays an important role in the separation and transport of photogenerated charges. Therefore, the NPG/CdS structure was investigated via high-angle annular dark-field (HAADF) scanning TEM (STEM). The sharp interfaces and the details of the atomic and lattice structures of CdS and Au at the junction of the two crystalline phases can be clearly observed(Fig. 2(a)) (the signals of light elements, such as S, are too weak to be distinctly observed under the HAADF mode).

Two sets of inter planar spacing of 2.0 Å in the NPG region are assigned to two orthogonal lattice planes, namely, the (020) and (002) planes of face-centered cubic (fcc) Au, whereas the spacings of 3.6 and 3.4 Å in the CdS NL correspond to the (010) and (002) lattice planes of wurtzite CdS, respectively. The crystal structures of NPG and NPG/CdS NHJs with different electrodeposition times were also confirmed via X-Ray diffraction (XRD) (Fig. S6 in the ESM). All the diffraction peaks are indexed to the face-centered cubic structure of Au and the hexagonal phase of CdS. The corresponding fast Fourier transform (FFT) pattern, which is precisely indexed in Fig. 2(e), provides further support for the above results and indicates the single-crystalline nature of NPG and CdS in the characterized region that serves to be in thermo-dynamic equilibrium for improving the stability of the material [46] and promoting charge mobility and carrier diffusion length [29, 47]. Moreover, the simulated atomic-level interface structure of the NHJ (see Fig. 2(b)) is nearly coincident with the actual boundary between CdS and Au, with only a tiny angular distortion (~2°) caused by the stress from the different interplanar spacings of the two crystalline phases. The ADF-STEM image displayed in Fig. 2(f), which is derived from the NPG/CdS interface region in Fig. 2(a), illustrates the arrangement of the Cd and

Au atoms in greater detail, yielding the corresponding EELS maps shown in Figs. 2(g)–2(i). Excitingly, Cd and S atoms can be clearly seen and easily distinguished by ultrahigh resolution from the atomic-scale EELS mapping results shown in Figs. 2(g) and 2(h), thereby providing decisive proof of the formation of a sharp and compact Au/CdS interface with high crystallinity.

As shown by the digital photographs in Fig. 1(a), the color of the electrode becomes much darker after the deposition of the CdS NL, which means that its photo-absorption is significantly enhanced. To investigate the LSPR properties of the NPG/CdS photoelectrode, the UV-Vis spectrum within the visible-light wavelength range was collected and compared with those of native NPG and CdS (see Fig. 3(a)). It can be seen that the NPG/CdS NHJ exhibits enhanced absorption over the entire visible-light region, especially between 490 and 650 nm. These result from the overlap of the resonant absorption of the gold film [38] and the absorption of the CdS segment resulting from 1Σ ($1\sigma e$–$1\sigma h$) and 1Π ($1\pi e$–$1\pi h$) exciton transitions corresponding to ~465.5 and ~393.5 nm, respectively (see the inset of Fig. 3(a)) between the discrete CBs and valence bands (VBs) of CdS. In addition, the NPG/CdS NHJ shows broader and stronger absorption over a larger wavelength band because of the plasmon–exciton interactions of NPG
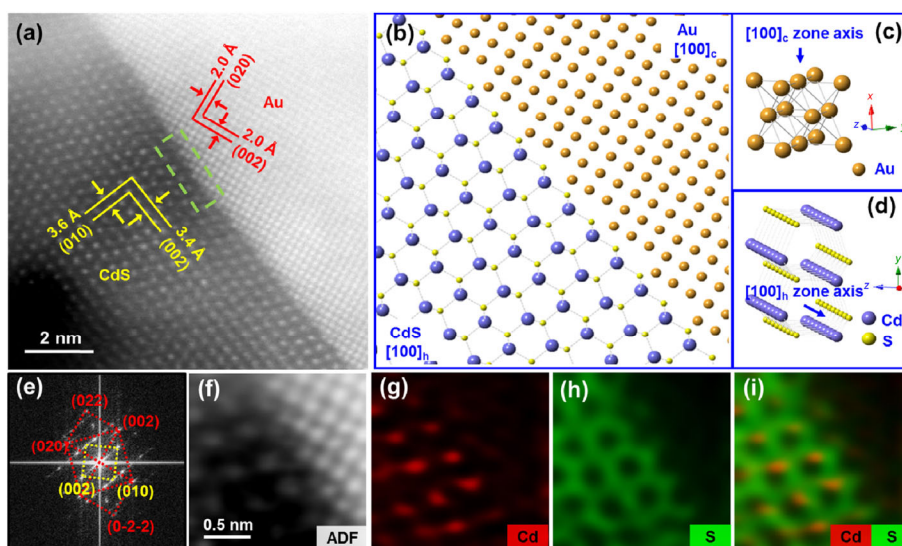

Figure 2 (a) HAADF-STEM image of NPG/CdS. (b) Simulated atomic-level structure consistent with (a). Zone-axis orientations and unit cell structures of (c) Au and (d) CdS. (e) FFT pattern corresponding to (a). (f) ADF-STEM image derived from the NPG/CdS interface. The corresponding EELS mapping results for (g) Cd and (h) S and (i) an overlay of both.

and CdS, and presents a significant red-shift from ~523 nm for NPG (orange line) to ~544 nm for NPG/CdS (red line). This phenomenon indicates that the NPG/CdS NHJ is photoactive within a very broad window of the solar spectrum relative to both the NPG and CdS components. Further studies (Fig. S7 in the ESM) demonstrate that LSPR is present only in NPG/CdS and not in Au/CdS, which implies that the nanoporous nature of the NPG plays a critical role in the generation of a strong LSPR signal.

To examine the spatial distribution of the LSPR modes in NPG, EELS experiments were performed and the results presented in Figs. 3(d)–3(i). The EEL spectra of an NPG slice (Fig. S8 in the ESM) revealed that the NPG structure supports multiple LSPR modes. The energies of these LSPR modes are bound to the standing wave limit of Au surface plasmons (2.4 eV) and span the visable-infrared spectroscopy (Vis-IR) range. More importantly, the comparison of EELS maps of the NPG/CdS NHJ (Figs. 3(h) and 3(i)) with those of NPG (Figs. 3(e) and 3(f)), which are obtained from 1.6 and 2.4 eV energy filters, reveals an evident reduction of EEL probability in the NHJ, indicating

plasmon energy transfer from NPG to CdS [22]. Femtosecond transient absorption (TA) spectroscopy was conducted to further investigate the charge energy and hot electron transfer behaviors between NPG and CdS. The 490 nm photo-bleaching (PB) signals (Fig. S9 in the ESM) in NPG/CdS and FTO/CdS samples originate from the filling of states close to the fundamental band gap of CdS. As shown in Fig. 3(b), a slower rise-in of the 490 nm PB signal in the NPG/CdS NHJ was observed than that in FTO/CdS sample. The slower rise-in signal indicates that CdS is absorbing the addition charges [48], likely hot electron transfer from NPG to CdS under the photoexcitation at λ = 400 nm [49]. Furthermore, a concomitant rise- decay behavior between the 490 and 500 nm PB signals in the NPG/CdS NHJ was shown in Fig. 3(c), which is a well-established signature of charge-energy transfer processes [50]. In the spectra, the 490 and 500 nm PB signals are characteristic signals for CdS (acceptor) and NPG (donor). This behavior states that the dynamics from the donor undergoes a fast decay while the dynamics from the acceptor undergoes a rise-in simultaneously. These two dynamic rise and decay
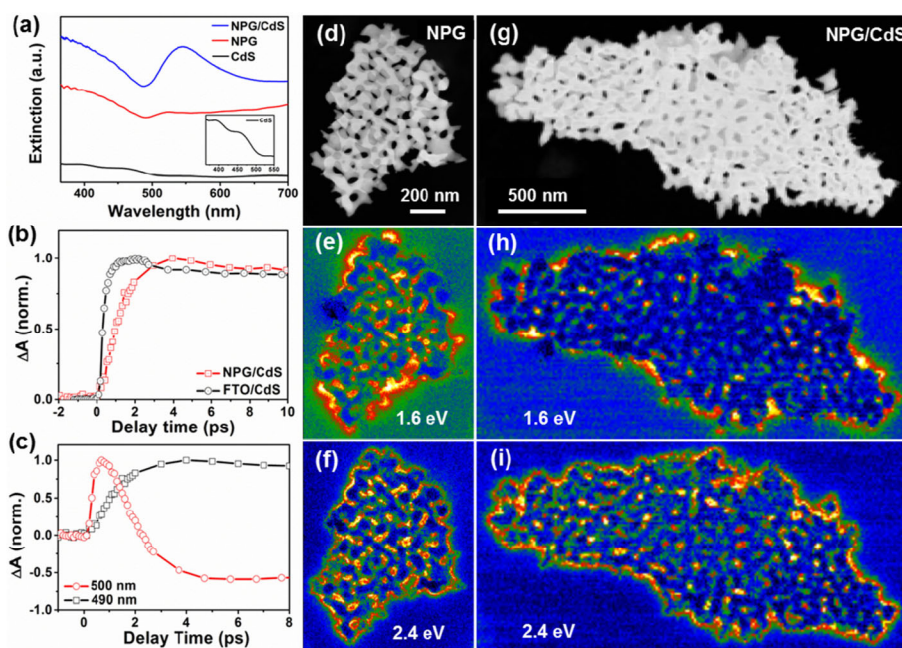

Figure 3 (a) UV-Vis absorption spectra of CdS, NPG, and NPG/CdS. (b) and (c) Transient absorption spectra of NPG/CdS NHJs and FTO/CdS excited at λ = 400 nm. (b) The rise-in dynamics monitored at 490 nm; (c) the concomitant rise-decay behavior observed in NPG/CdS NHJs. (d) ADF image of the NPG. (e) and (f) The corresponding plasmon maps of NPG in (d) obtained from 1.6 and 2.4 eV energy filters, respectively. (g) ADF image of the NPG/CdS. (h) and (i) The corresponding plasmon maps of NPG in (g) obtained from 1.6 and 2.4 eV energy filters, respectively.

processes have the same time scale [37, 49].

In a proof-of-concept experiment, the PEC-HE photocatalytic activity of NPG/CdS NHJs operating as photoanodes was investigated by monitoring their photocurrents. The transient photocurrent responses of NPG/CdS NHJs prepared with different deposition times (40–140 s) under visible-light irradiation were measured during repeated ON/OFF illumination cycles at 0 V vs. SCE (see Fig. S10 in the ESM). All the NHJs exhibited prompt and reproducible photocurrent responses between the interruption and restoration of the irradiation, indicating the rapid formation and effective separation of electron–hole pairs. The transient photocurrent density (J) of the NPG/CdS photoelectrode clearly presents a volcano shape with increasing electrodeposition time at 0 V vs. SCE. The NPG/CdS NHJ obtained with a deposition time of 110 s produces a maximum of approximately 1.04 mA·cm^{-2}. The increase in J during the early stage of electrodeposition may result from the strong coupling of the excitonic state of the CdS NL with the plasmonic mode of NPG. With increasing electrodeposition time, more CdS is formed that harvests incidentally scattered plasmonic photons and obtains SPR energy from NPG, creating more electron–hole pairs that can rapidly transfer. During the later stage of electrodeposition, the decrease in J can most likely be attributed to the CB level of the thicker CdS NL resulting in a decreased photoelectron injection force and a longer distance for the transmission of photoelectrons from CdS to NPG, which may lead to a greater probability of recombination in CdS. Another possible reason is that the pores of the NPG may be blocked by the thicker CdS layer, preventing the electrolyte from easily entering into the pores and resulting in a low capture efficiency of photoexcited holes. It should be noted that the photocurrent of NPG/CdS NHJ photo-electrodes can be readily enhanced by increasing their overall thickness to 200 or 400 nm, which allows J to achieve ~1.6 and 2.1 mA·cm^{-2}, respectively (see Fig. S11 in the ESM). The flexibility in the thickness and thus performance control of NPG/NHJ electrodes indicates their great potential for PEC water splitting.

To further demonstrate the advantages of the fabricated 3D NPG/CdS NHJs, the PEC-HE photo-catalytic activity of the NPG/CdS NHJ prepared with a deposition time of 110 s was compared with that of CdS deposited on Au foil (Au/CdS) and an FTO substrate (FTO/CdS). To rule out possible interferences, the amount of CdS was controlled to be nearly the same for all samples (Table S1 in the ESM). Besides, SEM images shown in Fig. S12 in the ESM confirms very similar morphology of the CdS overlayer in Au/CdS and NPG/CdS, as evidenced by uniform dispersion of small nanoparticles. As shown in Fig. 4(a), the photocurrent density of NPG/CdS is two and four times larger than that of Au/CdS and CdS, indicating that 3D NPG indeed provides better performance in terms of the formation, separation, and transfer of photogenerated charges, when compared with Au foil and FTO. The enhanced photo-current in NPG/CdS can be predominantly attributed to the plasmonic enhancement effect from NPG. EIS under irradiation further confirms the highly effective charge transfer in the NPG/CdS NHJ. The radii of the semicircles in the intermediate-frequency region, which are correlated with the electron transfer at the electrode–electrolyte interface and the charge-transfer resistance (R_{CT}), reflect the charge transfer efficiencies of the photocatalysts [32, 51]. As shown in Fig. 4(b), NPG/CdS, Au/CdS, and CdS, all show semicircular EIS diagrams in the form of Nyquist plots, and the NPG/CdS NHJ exhibits the smallest semicircle. Specifically, the R_{CT} of NPG/CdS NHJ is 602 Ω, which is much smaller than those of Au/CdS (820 Ω) and CdS (3,263 Ω), further demonstrates the more effective electron–hole pair separation and efficient interfacial electron transfer in the NPG/CdS NHJ. Moreover, an additional electric double-layer capacitor (C_{DL2}) is present in the equivalent electric circuit, which is a feature of porous electrodes [52]. The efficient transport of charge-carriers at the NHJ interface is further examined via applied bias photon-to-current efficiency and monochromatic IPCE measurements for NPG/CdS, Au/CdS, and FTO/CdS. As shown in Fig. S13 in the ESM, the NPG/CdS NHJ exhibits a larger improvement of IPCE value compared with Au/CdS in the overall visible-light region. The efficient separation and transport of photogenerated charges may be derived from the direct contact interface and highly conductive framework of NPG/CdS NHJs. The hydrogen evolution performance of NPG/CdS was evaluated at 0 V vs. SCE under 1-sun
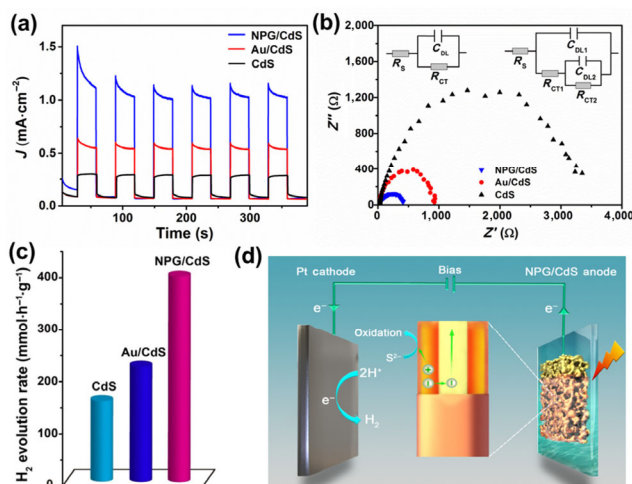
Figure 4 (a) Transient photocurrent densities (J) of NPG/CdS, Au/CdS, and CdS. (b) Nyquist EIS plots in the frequency range of 5,000 Hz to 50 mHz. (c) Hydrogen evolution rates for NPG/CdS, Au/CdS, and CdS. (d) Schematic illustration of a PEC-HE cell. All experiments were conducted at 0 V vs. SCE under visible-light irradiation from an Xe lamp (420 nm $< \lambda <$ 780 nm, 100 mW·cm^{-2}).

illumination by assuming a 100% Faradaic efficiency, and the result was compared with those for Au/CdS and CdS samples. During the hydrogen evolution process, the photogenerated electrons after separation from holes flow to the Pt counter electrode through the external circuit and take part in the half-reaction of water reduction into hydrogen (see Fig. 4(d)). As shown in Fig. 4(c), the hydrogen evolution rate for NPG/CdS was determined via gas chromatography to be 406 mmol·h^{-1}·g^{-1}, which is not only much faster than that for Au/CdS and FTO/CdS, but also very competitive compared to the reported photocatalysts (summarized in Table S2 in the ESM). These above results confirm the superiority of the NPG/CdS NHJ structures as photoelectrodes for PEC-HE.

To fully evaluate the PEC performance of the NPG/CdS NHJ, the photostability of NPG/CdS and CdS was measured under visible-light irradiation for 10^4 s. The photocurrent density of the NPG/CdS NHJ dropped by only 23% after 10^4 s of irradiation, which is far superior to the 67% decrease observed for the CdS over the same time period (as shown in Figs. 5(a) and 5(b)). In general, decreased photoactivity and Cd ion leakage are consequences of the oxidation of S ions by photogenerated holes with strong oxidation power, followed by the release of Cd ions into the

solution, that is, the photocorrosion of the CdS. This photocorrosion greatly limits the application of non-oxide semiconductors as photoelectrode materials [2, 14, 53]. The results reported above were clarified by XPS investigations of the elemental compositions, chemical statuses, and electronic states of the photoanodes before and after 10^4 s of irradiation. As shown in Fig. 5(e), the Cd 3d spectrum features peaks at 412.2 (Cd 3d$_{3/2}$) and 405.5 eV (Cd 3d$_{5/2}$) assigned to Cd^{2+}, which exhibit no energy change before and after irradiation for 10^4 s. The doublet structure of the S 2p, with binding energies of 163.1 and 161.9 eV deriving from 2p$_{1/2}$ and 2p$_{3/2}$ (a spin-orbit splitting of 1.2 eV [54]), respectively, also remains unchanged (Fig. 5(d)). These findings demonstrate that the conformal NHJ is stable when subjected to irradiation, with substantially suppressed photocorrosion. Significantly, after irradiation, the binding energy peaks of Au 4f$_{7/2}$ at 84.1 and 87.8 eV shift upward to 84.5 and 88.2 eV, respectively (Fig. 5(c)), which is attributed to the oxidation of Au, signifying the formation of Au–S bond echoes with the S 2p$_{3/2}$ signal at 161.9 eV [11, 55]. Accordingly, NPG likely plays a vital role as a scavenger, capturing the photo-excited holes in the VB of the CdS; then, the resulting Au$^+$ reacts with S^{2-} from the sacrificial agents to produce Au–S bonds, thereby effectively preventing the photocorrosion of the CdS and enabling the observed steady PEC-HE performance. By contrast, a downward shift in the Cd 3d$_{5/2}$ peak energy from 405.4 to 404.8 eV can be observed for CdS, which implies the oxidation of the CdS after 10^4 s of irradiation (Fig. 5(f)). This photocorrosion of CdS leads to a severe decrease in the photocurrent density. This study demonstrates that 3D porous NPG/CdS NHJs operating as photoelectrodes show enhanced and stable PEC-HE performance relative to both Au/CdS and CdS. This remarkable PEC-HE performance can be primarily attributed to the following reasons: (1) the multiple scattering of plasmonic photons by patterned NPG leads to increased light absorption, resulting in the formation of more electron-hole pairs [17, 18]; (2) the localized and amplified near-field E-field from NPG promotes the coupling between plasmons and excitons, by increasing the generation rate of electron–hole pairs [20, 43, 56]; (3) direct hot electron transfer from NPG
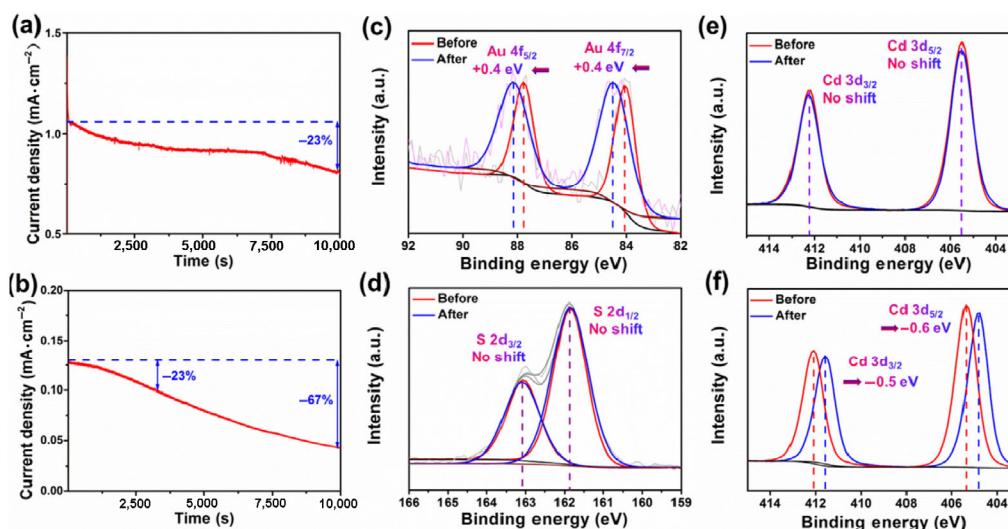
Figure 5 Photostability of (a) NPG/CdS and (b) CdS under 10^4 s of visible-light irradiation from a Xe lamp (420 nm $< \lambda <$ 780 nm, 100 mW·cm^{-2}). XPS spectra before (red lines) and after (blue lines) irradiation for 10^4 s, (c) Au 4f, (d) S 2p, and (e) Cd 3d of NPG/CdS, and (f) Cd 3d of CdS.

to CdS provides excess energy for hydrogen evolution [27, 51, 57]; (4) the direct contact at the interface between NPG and CdS NL and highly conductive framework of NHJ are beneficial for electron–hole pair separation and transport [17, 28]; and (5) NPG also plays a vital role as a hole scavenger to prevent the photocorrosion of CdS [55].

4   Conclusions

In conclusion, we have successfully fabricated ultrathin integrated 3D NHJ photoelectrodes via a facile and eco-friendly electrodeposition process, by directly coating a CdS NL onto NPG. This unique NGP/CdS NHJ offers a number of impressive advantages, including simple and mass fabrication of photoelectrode, flexible, ultrathin, translucent, and atomic-level contact interface, which are highly desirable for the practical use of PEC hydrogen generation. By taking advantage of the nano- and macro-structures of NPG and the strong plasmon–exciton interactions between NPG and CdS, the NPG/CdS NHJ photoelectrode with just ~100 nm overall thickness exhibits a favorable photocurrent density of 1.04 mA·cm^{-2} and an impressive hydrogen evolution rate. Moreover, the photostability of NPG/CdS over 10^4 s of irradiation is far superior to that of bare CdS. This flexible 3D integrated NHJ

photoanode, with its excellent photocatalytic performance, shows promise for a wide variety of applications in solar photovoltaic cells and wearable optoelectronic devices. More importantly, the facile fabrication process for the integrated 3D NHJ photoelectrodes developed here may be a key innovation for the development of solar energy conversion technologies.

Acknowledgements

Electronic Supplementary Material: Supplementary material (additional information and figures, including additional characterization data for samples and the

hydrogen evolution rate calculation) is available in the online version of this article at https://doi.org/10.1007/s12274-017-1821-y.

References

[1] Grätzel, M. Photoelectrochemical cells. *Nature* **2001**, *414*, 338–344.

[2] Li, Z. S.; Luo, W. J.; Zhang, M. L.; Feng, J.Y.; Zou, Z. G. Photoelectrochemical cells for solar hydrogen production: Current state of promising photoelectrodes, methods to improve their properties, and outlook. *Energy Environ. Sci.* **2013**, *6*, 347–370.

[3] Scheuermann, A. G.; Lawrence, J. P.; Kemp, K. W.; Ito, T.; Walsh, A.; Chidsey, C. E. D.; Hurley, P. K.; McIntyre, P. C. Design principles for maximizing photovoltage in metal-oxide-protected water-splitting photoanodes. *Nat. Mater.* **2016**, *15*, 99–105.

[4] Moniz, S. J. A.; Shevlin, S. A.; Martin, D. J.; Guo, Z. X.; Tang, J. W. Visible-light driven heterojunctionphotocatalysts for water splitting-a critical review. *Energy Environ. Sci.* **2015**, *8*, 731–759.

[5] Yang, J. H.; Wang, D. E.; Han, H. X.; Li, C. Roles ofcocatalysts in photocatalysis and photoelectrocatalysis. *Acc. Chem. Res.* **2013**, *46*, 1900–1909.

[6] Sun, Z. J.; Zheng, H. F.; Li, J. S.; Du, P. W. Extraordinarily efficient photocatalytic hydrogen evolution in water using semiconductor nanorods integrated with crystalline Ni_2P cocatalysts. *Energy Environ. Sci.* **2015**, *8*, 2668–2676.

[7] Zhuang, T. T.; Liu, Y.; Li, Y.; Zhao, Y.; Wu, L.; Jiang, J.; Yu, S. H. Integration of semiconducting sulfides for full-spectrum solar energy absorption and efficient charge separation. *Angew. Chem., Int. Ed.* **2016**, *55*, 6396–6400.

[8] Wei, Y. K.; Su, J. Z.; Wan, X. K.; Guo, L. J.; Vayssieres, L. Spontaneous photoelectric field-enhancement effect prompts the low cost hierarchical growth of highly ordered heteronanostructures for solar water splitting. *Nano Res.* **2016**, *9*, 1561–1569.

[9] Wu, F. L.; Cao, F. R.; Liu, Q.; Lu, H.; Li, L. Enhancing photoelectrochemical activity with three-dimensional p-CuO/n-ZnO junction photocathodes. *Sci. China Mater.* **2016**, *59*, 825–832.

[10] Kalisman, P.; Nakibli, Y.; Amirav, L. Perfect photon-to-hydrogen conversion efficiency. *Nano Lett.* **2016**, *16*, 1776–1781.

[11] Chen, X. X.; Li, Y. P.; Pan, X. Y.; Cortie, D.; Huang, X. T.; Yi, Z. G. Photocatalytic oxidation of methane over silver decorated zinc oxide nanocatalysts. *Nat. Commun.* **2016**, *7*, 12273.

[12] Zhang, J. M.; Jin, X.; Morales-Guzman, P. I.; Yu, X.; Liu, H.; Zhang, H.; Razzari, L.; Claverie, J. P. Engineering the absorption and field enhancement properties of Au-TiO_2 nanohybrids via whispering gallery mode resonances for photocatalytic water splitting. *ACS Nano* **2016**, *10*, 4496–4503.

[13] Hu, D. Y.; Diao, P.; Xu, D.; Wu, Q. Y. Gold/WO_3 nano-compositephotoanodes for plasmonic solar water splitting. *Nano Res.* **2016**, *9*, 1735–1751.

[14] Xian, J. J.; Li, D. Z.; Chen, J.; Li, X. F.; He, M.; Shao, Y.; Yu, L. H.; Fang, J. L. TiO_2 nanotube array-graphene-CdS quantum dots composite film in Z-scheme with enhanced photoactivity and photostability. *ACS Appl. Mater. Interfaces* **2014**, *6*, 13157–13166.

[15] Kofuji, Y.; Isobe, Y.; Shiraishi, Y.; Sakamoto, H.; Tanaka, S.; Ichikawa, S.; Hirai, T. Carbon nitride-aromatic diimide-graphenenanohybrids: Metal-free photocatalysts for solar-to-hydrogen peroxide energy conversion with 0.2% efficiency. *J. Am. Chem. Soc.* **2016**, *138*, 10019–10025.

[16] Liu, W. X.; Liu, Z. Y.; Wang, G. N.; Sun, X. M.; Li, Y. P.; Liu, J. F. Carbon coated Au/TiO_2 mesoporous microspheres: A novel selective photocatalyst. *Sci. China Mater.* **2017**, *60*, 438–448.

[17] Li, J. T.; Cushing, S. K.; Zheng, P.; Meng, F. K.; Chu, D.; Wu, N. Q. Plasmon-induced photonic and energy-transfer enhancement of solar water splitting by a hematite nanorod array. *Nat. Commun.* **2013**, *4*, 2651.

[18] Cushing, S. K.; Wu, N. Q. Plasmon-enhanced solar energy harvesting. *Electrochem. Soc. Interface* **2013**, *22*, 63–67.

[19] Thomann, I.; Pinaud, B. A.; Chen, Z. B.; Clemens, B. M.; Jaramillo, T. F.; Brongersma, M. L. Plasmon enhanced solar-to-fuel energy conversion. *Nano Lett.* **2011**, *11*, 3440–3446.

[20] Linic, S.; Christopher, P.; Ingram, D. B. Plasmonic-metal nanostructures for efficient conversion of solar to chemical energy. *Nat. Mater.* **2011**, *10*, 911–921.

[21] Xing, X. L.; Liu, R. J.; Yu, X. L.; Zhang, G. J.; Cao, H. B.; Yao, J. N.; Ren, B. Z.; Jiang, Z. X.; Zhao, H. Self-assembly of CdS quantum dots with polyoxometalate encapsulated gold nanoparticles: Enhanced photocatalytic activities. *J. Mater. Chem. A* **2013**, *1*, 1488–1494.

[22] Li, G. L.; Cherqui, C.; Bigelow, N. W.; Duscher, G.; Straney, P. J.; Millstone, J. E.; Masiello, D. J.; Camden, J. P. Spatially mapping energy transfer from single plasmonic particles to semiconductor substrates via STEM/EELS. *Nano Lett.* **2015**, *15*, 3465–3471.

[23] Smith, J. G.; Faucheaux, J. A.; Jain, P. K. Plasmon resonances for solar energy harvesting: A mechanistic outlook. *Nanotoday* **2015**, *10*, 67–80.

[24] Warren, S. C.; Thimsen, E.Plasmonic solar water splitting. *Energy Environ. Sci.* **2012**, *5*, 5133–5146.

[25] Maaroof, A. I.; Lee, H.; Heo, K.; Park, J.; Cho, D.; Lee, B. Y.; Seong, M. J.; Hong, S. Plasmon-exciton interactions in hybrid structures of au nanohemispheres and CdS nanowires for improved photoconductive devices. *J. Phys. Chem. C* **2013**, *117*, 24543–24548.

[26] Li, M.; Yu, X. F.; Liang, S.; Peng, X. N.; Yang, Z. J.; Wang, Y. L.; Wang, Q. Q. Synthesis of Au-CdS core–shell hetero-nanorods with efficient exciton–plasmon interactions. *Adv. Funct. Mater.* **2011**, *21*, 1788–1794.

[27] Wu, K. F.; Rodríguez-Córdoba, W. E.; Yang, Y.; Lian, T. Q. Plasmon-induced hot electron transfer from the Au tip to CdSrod in CdS-Au nanoheterostructures. *Nano Lett.* **2013**, *13*, 5255–5263.

[28] Wang, X. T.; Liow, C.; Qi, D. P.; Zhu, B. W.; Leow, W. R.; Wang, H.; Xue, C.; Chen, X. D.; Li, S. Z. Programmable photo-electrochemical hydrogen evolution based on multi-segmented CdS-Au nanorod arrays. *Adv. Mater.* **2014**, *26*, 3506–3512.

[29] Saliba, M.; Zhang, W.; Burlakov, V. M.; Stranks, S. D.; Sun, Y.; Ball, J. M.; Johnston, M. B.; Goriely, A.; Wiesner, U.; Snaith, H. J.Plasmonic-induced photon recycling in metal halide perovskite solar cells. *Adv. Funct. Mater.* **2015**, *25*, 5038–5046.

[30] Zheng, X. L.; Song, J. P.; Ling, T.; Hu, Z. P.; Yin, P. F.; Davey, K.; Du, X. W.; Qiao, S. Z. Strongly coupled nafion molecules and ordered porous CdS networks for enhanced visible-light photoelectrochemical hydrogen evolution. *Adv. Mater.* **2016**, *28*, 4935–4942.

[31] Chen, M.; Gu, J. J.; Sun, C.; Zhao, Y. X.; Zhang, R. X.; You, X. Y.; Liu, Q. L.; Zhang, W.; Su, Y. S.; Su, H. L. et al. Light-driven overall water splitting enabled by a photo-dember effect realized on 3D plasmonic structures. *ACS Nano* **2016**, *10*, 6693–6701.

[32] Hou, Y.; Zuo, F.; Dagg, A.; Feng, P. Y. A three-dimensional branched cobalt-doped α-Fe$_2$O$_3$ nanorod/MgFe$_2$O$_4$ hetero-junction array as a flexible photoanode for efficient photoelectrochemical water oxidation. *Angew. Chem., Int. Ed.* **2013**, *125*, 1248–1252.

[33] Yan, L. J.; Liu, Y.; Yan, Y. N.; Wang, L. F.; Han, J.; Wang, Y. N.; Zhou, G. W.; Swihart, M. T.; Xu, X. H. Improved plasmon-assisted photoelectric conversion efficiency across entire ultraviolet-visible region based on antenna-on zinc oxide/silver three-dimensional nanostructured films. *Nano Res.* **2017**. DOI 10.1007/s12274-017-1663-7.

[34] Law, M.; Greene, L. E.; Johnson, J. C.; Saykally, R.; Yang, P. D. Nanowire dye-sensitized solar cells. *Nat. Mater.* **2005**, *4*, 455–459.

[35] Ye, M. D.; Xin, X. K.; Lin, C. J.; Lin, Z. Q. High efficiency dye-sensitized solar cells based on hierarchically structured nanotubes. *Nano Lett.* **2011**, *11*, 3214–3220.

[36] Chen, W. T.; Yang, T. T.; Hsu, Y. J. Au-CdS core–shell nanocrystals with controllable shell thickness and photoin-duced charge separation property. *Chem. Mater.* **2008**, *20*, 7204–7206.

[37] Yin, X. L.; He, G. Y.; Sun, B.; Jiang, W. J.; Xue, D. J.; Xia, A. D.; Wan, L. J.; Hu, J. S. Rational design and electron transfer kinetics of MoS$_2$/CdSnanodots-on-nanorods for efficient visible-light-driven hydrogen generation. *Nano Energy* **2016**, *28*, 319–329.

[38] Lang, X. Y.; Qian, L. H.; Guan, P. F.; Zi, J.; Chen, M. W. Localized surface Plasmon resonance of nanoporous gold. *Appl. Phys. Lett.* **2011**, *98*, 093701.

[39] Jia, C. C.; Yin, H. M.; Ma, H. Y.; Wang, R. Y.; Ge, X. B.; Zhou, A. Q.; Xu, X. H.; Ding, Y. Enhanced photoelectrocatalytic activity of methanol oxidation on TiO$_2$-decorated nanoporous gold. *J. Phys. Chem. C* **2009**, *113*, 16138–16143.

[40] Jia, C. C.; Li, X. X.; Xin, N.; Gong, Y.; Guan, J. X.; Meng, L. A.; Meng, S.; Guo, X. F. Interface-engineered plasmonics in metal/semiconductor heterostructures. *Adv. Energy Mater.* **2016**, *6*, 1600431.

[41] Zhang, L.; Chen, L. Y.; Liu, H. W.; Hou, Y.; Hirata, A.; Fujita, T.; Chen, M. W. Effect of residual silver on surface-enhanced Raman scattering of dealloyednanoporousgold. *J. Phys. Chem. C* **2011**, *115*, 19583–19587.

[42] Zhang, W. Q.; Rahmani, M.; Niu, W. X.; Ravaine, S.; Hong, M. H.; Lu, X. M. Tuning interior nanogaps of double-shelled Au/Ag nanoboxes for surface-enhanced Raman scattering. *Sci. Rep.* **2015**, *5*, 8382.

[43] Achermann, M. Exciton–plasmon interactions in metal-semiconductor nanostructures. *J. Phys. Chem. Lett.* **2010**, *1*, 2837–2843.

[44] Ding, Y.; Kim, Y. J.; Erlebacher, J. Nanoporous gold leaf: "Ancient technology"/advanced material. *Adv. Mater.* **2004**, *16*, 1897–1900.

[45] Li, J.; Yin, H. M.; Li, X. B.; Okunishi, E.; Shen, Y. L.; He, J.; Tang, Z. K.; Wang, W. X.; Yücelen, E.; Li, C. et al. Surface evolution of a Pt-Pd-Au electrocatalyst for stable oxygen reduction. *Nat. Energy* **2017**, *2*, 17111

[46] Fakharuddin, A.; Di Giacomo, F.; Palma, A. L.; Matteocci, F.; Ahmed, I.; Razza, S.; D'Epifanio, A.; Licoccia, S.; Ismail, J.; Di Carlo, A. et al. Vertical TiO$_2$ nanorods as a medium for stable and high-efficiency perovskite solar modules. *ACS Nano* **2015**, *9*, 8420–8429.

[47] Xiao, Z. G.; Bi, C.; Shao, Y. C.; Dong, Q. F.; Wang, Q.; Yuan, Y.B.; Wang, C. G.; Gao, Y. L.; Huang, J. S. Efficient, high yield perovskite photovoltaic devices grown by inter-diffusion of solution-processed precursor stacking layers. *Energy Environ. Sci.* **2014**, *7*, 2619–2623.

[48] Ibrahim, I.; Lim, H. N.; Abou-Zied, O. K.; Huang, N. M.; Estrela, P.; Pandikumar, A. Cadmium sulfide nanoparticles decorated with Au Quantum dots as ultrasensitive photo-electrochemical sensor for selective detection of copper(II) ions. *J. Phys. Chem. C* **2016**, *120*, 22202–22214.

[49] Khon, E.; Mereshchenko, A.; Tarnovsky, A. N.; Acharya, K.; Klinkova, A.; Hewa-Kasakarage, N. N.; Nemitz, I.; Zamkov, M. Suppression of the plasmon resonance in Au/CdS colloidal nanocomposites. *Nano Lett.* **2011**, *11*, 1792–1799.

[50] Maity, P.; Debnath, T.; Ghosh, H. N. Ultrafast hole- and electron-transfer dynamics in CdS-dibromofluorescein (DBF) supersensitized quantum dot solar cell materials. *J. Phys. Chem. Lett.* **2013**, *4*, 4020–4025.

[51] Jana, A.; Bhattacharya, C.; Datta, J. Enhanced photo-electrochemical activity of electro-synthesized CdS-Bi$_2$S$_3$ composite films grown with self-designed cross-linked structure. *Electrochim. Acta* **2010**, *55*, 6553–6562.

[52] Iozzo, D. A. B.; Tong, M.; Wu, G.; Furlani, E. P. Numerical analysis of electric double layer capacitors with mesoporous electrodes: Effects of electrode and electrolyte properties. *J. Phys. Chem. C* **2015**, *119*, 25235–25242.

[53] Tang, Y. H.; Hu, X.; Liu, C. B. Perfect inhibition of CdS photocorrosion by graphene sheltering engineering on TiO$_2$ nanotube array for highly stable photocatalytic activity. *Phys. Chem. Chem. Phys.* **2014**, *16*, 25321–25329.

[54] Duwez, A.S. Exploiting electron spectroscopies to probe the structure and organization of self-assembled monolayers: a review. *J. ElectronSpectrosc. Relat.Phenom.* **2004**, *134*, 97–138.

[55] Ma, X.; Zhao, K.; Tang, H. J.; Chen, Y.; Lu, C. G.; Liu, W.; Gao, Y.; Zhao, H. J.; Tang, Z. Y. New insight into the role of gold nanoparticles in Au@CdScore–shell nanostructures for hydrogen evolution. *Small* **2014**, *10*, 4664–4670.

[56] Murray, W. A.; Barnes, W. L.Plasmonic materials. *Adv. Mater.* **2007**, *19*, 3771–3782.

[57] Wu, K.; Chen, J.; McBride, J. R.; Lian, T. Efficient hot-electron transfer by a plasmon-induced interfacial charge-transfer transition. *Science* **2015**, *349*, 632–635.